Non-Hermitian optics in atomic systems

View the article online for updates and enhancements.

Topical Review

Non-Hermitian optics in atomic systems

Zhaoyang Zhang[1] , Danmeng Ma[1], Jiteng Sheng[2], Yiqi Zhang[1],
Yanpeng Zhang[1] and Min Xiao[3,4]

[1] Key Laboratory for Physical Electronics and Devices of the Ministry of Education & Shaanxi Key Lab of Information Photonic Technique, Xi'an Jiaotong University, Xi'an, 710049, People's Republic of China
[2] State Key Laboratory of Precision Spectroscopy, East China Normal University, Shanghai, 200062, People's Republic of China
[3] Department of Physics, University of Arkansas, Fayetteville, AR 72701, United States of America
[4] National Laboratory of Solid State Microstructures and School of Physics, Nanjing University, Nanjing 210093, People's Republic of China

E-mail: ypzhang@mail.xjtu.edu.cn and mxiao@uark.edu

Abstract

A wide class of non-Hermitian Hamiltonians can possess entirely real eigenvalues when they have parity-time (PT) symmetric potentials. Recently, this family of non-Hermitian systems has attracted considerable attention in diverse areas of physics due to their extraordinary properties, especially in optical systems based on solid-state materials, such as coupled gain–loss waveguides and microcavities. Considering the desired refractive index can be effectively manipulated through atomic coherence, it is important to realize such non-Hermitian optical potentials and further investigate their distinct properties in atomic systems. In this paper, we review the recent theoretical and experimental progress of non-Hermitian optics with coherently prepared multi-level atomic configurations. The realizations of (anti-) PT symmetry with different schemes have extensively demonstrated the special optical properties of non-Hermitian optical systems with atomic coherence.

(Some figures may appear in colour only in the online journal)

1. Introduction

It was discovered with fundamental importance that a wide class of complex non-Hermitian Hamiltonians obeying parity-time (PT) symmetry can possess entirely real eigenvalues, which was generally viewed as an exclusive property in Hermitian systems [1]. This counter-intuitive claim has rendered a great success in the theoretical development of non-Hermitian Hamiltonians related to PT symmetry [1–3]. One intriguing property of such PT-symmetric systems is an abrupt phase transition at a certain critical threshold. Once a parameter controlling the degree of non-Hermiticity goes beyond the PT-symmetry breaking threshold, namely, the phase transition point, the corresponding spectrum ceases to be real and starts to become complex [4–6]. The notion of PT

symmetry was experimentally demonstrated only after recognizing that the refractive index in optics can provide an effective solution to implement the required potential for PT-symmetric concepts [4, 5, 7–9]. What facilitates this possibility is the mathematical similarity between the quantum–mechanical Schrödinger equation and the paraxial optical wave equation, in which the spatially symmetric (even) real and anti-symmetric (odd) imaginary parts of the complex PT-symmetric potential exactly correspond to the real (dispersion) and imaginary (gain/absorption) parts of the refractive index profiles in optics, respectively. Consequently, a necessary, but not sufficient, condition for realizing PT symmetry in optics is that the real part and its imaginary counterpart of the refractive index n must be even and odd functions of the spatial position ($n(x) = n^*(-x)$), respectively [3, 5]. The odd
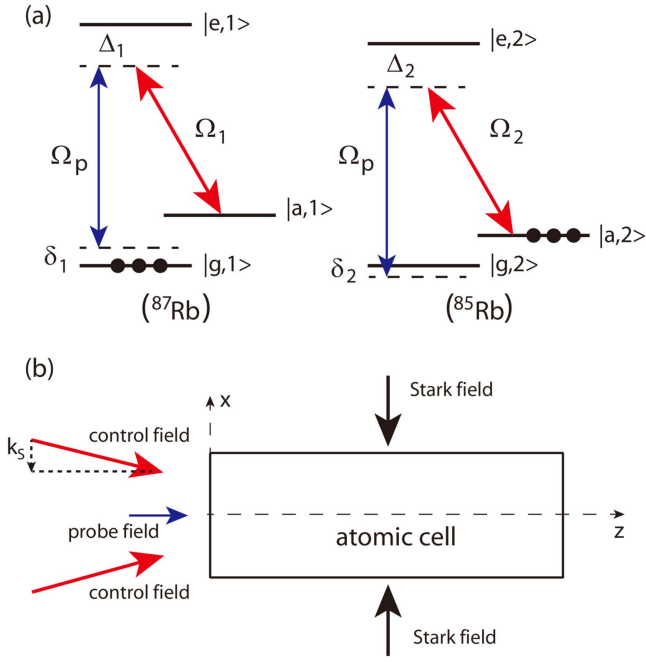
Figure 1. (a) Two Λ-type three-level excitation schemes for achieving a PT-symmetric potential. The initially populated states (i.e. $|g, 1\rangle$ and $|a, 2\rangle$) are indicated by the black dots. (b) Proposed experimental arrangement. Reprinted figure with permission from [34], Copyright (2013) by the American Physical Society.

imaginary index indicates the spatially extended gain and loss, which are responsible for introducing the non-Hermiticity into the optical systems.

In recent years, significant progresses regarding PT symmetry physics have been theoretically and experimentally achieved in various optical settings by balancing the simultaneous gain and loss [8–30]. The related studies have revealed many striking properties including non-Hermiticity-modulated Bloch oscillation [8, 9], unidirectional invisibility [15–18], perfect absorbers [21, 22], non-Hermitian solitons [23], topological insulators [24], enhancement of the sensitivity of optical detectors [27], and building lasers [28, 29] in PT-symmetric optical configurations. Most of these achievements, particularly in experiment, are finished in solid-state materials.

Inspired by the recent academic achievements of PT-symmetric optics and considering that coherent multi-level atomic gases are quite efficient in synthesizing desired refractive index profiles [31, 32], the constructions of PT-symmetric optical potentials have been predicted based on different atomic configurations [33–37]. Due to their natural attributes such as the laser-induced atomic coherence (introducing modifiable absorption, gain, and dispersion/nonlinearity), PT symmetry established in atomic media can have certain advantages over solid-state materials. On one hand, PT symmetry in atomic media can possess real-time observations, reconfigurable capability and effective controllability with multiple tunable parameters, and the underlying physical mechanisms can be investigated under various parametric conditions. On the other hand, by taking advantage of the interactions between non-Hermatian optical

potential and coherence-induced nonlinearity, many exotic effects have been theoretically studied, covering defect modes [38], solitons in nonlinear lattices [39] and unidirectional light transmission [40], Particularly, the development of electromagnetically induced transparency (EIT) [41] technique has made such traveling effects of light through non-Hermitian nonlinear optical systems be relatively easy to be observed and controlled in multi-level atomic systems [42].

In this article, we present a comprehensive review on the recent achievements of non-Hermitian optics in coherently-prepared atomic gases. In theory, we summarize the different physical schemes for realizing non-Hermitian optical systems and the predicted interesting optical properties in corresponding atomic settings. In experiment, we discuss two exciting progresses including the gain–loss modulated PT-symmetric optical lattices and anti-PT-symmetric potential (where $n(x) = -n^*(-x)$) generated in two optically-induced waveguides coupled via moving atoms. Particularly, in order to clearly explain how to experimentally construct PT-symmetric lattices, we also introduce the spatially periodical coherent optical effect in atomic settings. Finally, we end the review with a short summary.

2. Non-Hermitian optical potentials in multi-level atomic configurations

By utilizing the coherent nature of multi-level atomic media, various schemes based on different physical mechanisms (with different energy-level structures) such as Raman resonances and EIT technique are adopted to construct desired non-Hermitian optical potentials. In the following, we will present the features of non-Hermitian optical potentials generated in different atomic settings.

2.1. PT symmetry in a system of three-level atoms

The first scheme for creating PT symmetry based on atomic coherence is suggested in a three-level medium with a mixture of ^{85}Rb and ^{87}Rb, as shown in figure 1(a). The isotopes of rubidium atoms are coherently driven into a Λ-type configuration by one probe field $\boldsymbol{E}_p$ (frequency ω_p, electric-field intensity E_p) together with a controlling field $\boldsymbol{E}_s$ (ω_s, E_s) ($s = 1$, 2 represents the respective level in ^{85}Rb and ^{87}Rb). The Λ-type system consists of two ground-state levels ($|a, s\rangle$ and $|g, s\rangle$) and one excited level $|e, s\rangle$. The weak $\boldsymbol{E}_p$ and strong $\boldsymbol{E}_s$ (propagating along the same z direction) are introduced to connect the transitions $|g, s\rangle \leftrightarrow |e, s\rangle$ and $|a, s\rangle \leftrightarrow |e, s\rangle$, respectively. The controlling field is far from the resonance and the condition $\Delta_s \gg \Omega_s$ is satisfied, where Ω_s is the half Rabi frequency of $\boldsymbol{E}_s$ and $\Delta_s = \omega_{e,s} - \omega_{a,s} - \omega_s$ is one-photon detuning. By properly setting the two-photon detuning defined as $\delta_s = \omega_{e,s} - \omega_{g,s} - (\omega_p - \omega_s)$, the respective absorption and gain can be obtained on the probe field in ^{85}Rb and ^{87}Rb. The desired gain–loss profile is generated by modulating the spatial distribution of the one-photon detuning with a Stark field introduced.

J. Phys. B: At. Mol. Opt. Phys. **51** (2018) 072001

Topical Review

Next, the proper parameters are chosen to balance the gain and loss coefficients to satisfy the requirement condition $n(x) = n^*(-x)$ for PT symmetry. For achieving the desired spatial distribution of the index experienced by E_p, a strong far-detuned Stark field is incident into the medium to manipulate the one-photon detuning $\Delta_s(x)$ by controlling the Stark shifts of energy levels, considering that the controlling field affects both the one- and two-photon detunings. During the calculation, the difference of Stark shifts between the two ground sublevels is assumed to have no effect on the results. Then the two-photon detuning δ_s is immune to the influence from the Stark field, while the one-photon detuning is modified as $\Delta_s(x) = \Delta_s - (\alpha_{e,s} - \alpha_{g,s})E_s^2(x)/(4\hbar)$. As a result, the Stark field can effectively modulate the spatial arrangement of Δ_s without affecting the two-photon detuning.

The susceptibility χ of the medium can be obtained through the density-matrix equations (describing the interaction between the incident lasers and the medium) under the rotating-wave approximation and the paraxial approximation [43]. Considering the relations $\chi = \chi' + i\chi''$, $n = \sqrt{1 + \chi} \approx 1 + \chi/2$ and $n = n_0 + n_R + in_I$, the real and imaginary components of the index are given as $n_R \approx \frac{1}{2}\chi' = \frac{N\mu_{eg}}{\varepsilon_0 E_p}\mathrm{Re}(\rho_{eg})$ and $n_I \approx \frac{1}{2}\chi'' = \frac{N\mu_{eg}}{\varepsilon_0 E_p}\mathrm{Im}(\rho_{eg})$. Here, $n_0 = 1$ is the original index of the medium. The first step is to choose proper $\Omega_s(x)$ and $\Delta_s(x)$ by defining a 'seed' shape of the susceptibility $\chi^{sd}(x, \varepsilon_j, \eta)$ and then computing the analytical solutions for $\Omega_s^{sd}(x, \varepsilon_j, \eta)$ and $\Delta_s^{sd}(x, \varepsilon_j, \eta)$, where ε_j and η are the permittivity and the ratio between species densities, respectively. Based on the obtained χ_p, one can construct the spatial distribution of the $n(x)$ with the positive and negative imaginary parts representing respective loss and gain. The second step is to minimize the error by the controlling parameters ε_j and η. Due to the strong Doppler broadening effect [41], the far-off-resonant co-propagating controlling beams with the same frequency are adopted to establish the non-Hermitian structure. In the theoretical computation, the authors take the assumption that the controlling fields are two parallel plane waves with the same wavevector (x-component) of $k_a = 2\pi/\lambda_a$, (i.e. the Stark field wavevector). As a result, the finally obtained seed solution is $\chi^{sd} = \varepsilon_0 + \varepsilon_1\cos\xi + i\varepsilon_2\sin\xi$, where $\xi = k_a x$. The final step is to solve the expressions of the Rabi frequency Ω_s and the Stark-field amplitude E_a from equation $\chi_p(\Omega_s^{sd}, \Delta_s^{sd})$. As a result, the desired index satisfying $n(x) = n^*(-x)$ is established in the mixture of ^{85}Rb and ^{87}Rb. By changing the mutual concentration of the species, the described procedure can be 'structurally stable'.

By properly setting the sign of the two-photon detuning, which can modify the absorption/dispersion features of the probe field, the system can be PT-symmetric or non-PT-symmetric one. The propagation of an input Gaussian beam can be distinctly different for the two cases. One clear difference is that the propagation distance is longer in the PT-symmetric system, as shown in figure 2. The rapid consumption of the probe field in the non-PT-symmetric case is that its energy is exhausted in the dissipative medium.
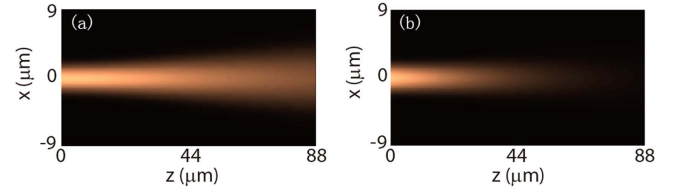

Figure 2. Propagation patterns of the probe light in the gases with (a) and without (b) PT-symmetric refractive indices. Reprinted figure with permission from [34], Copyright (2013) by the American Physical Society.
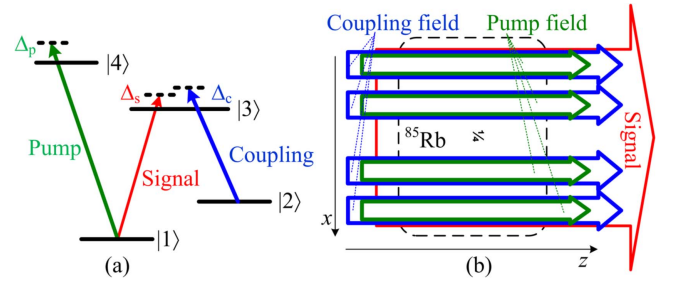

Figure 3. (a) The four-level N-type atomic configuration for obtaining PT-symmetric refractive index. (b) The spatial arrangement of the involved three fields inside the medium. z represents the propagation direction of lights, and x is transverse direction.

Further, by adding more controlling parameters, the system can also be potentially employed to demonstrate the nonlinear PT-symmetric properties [39, 44], as well as the combined linear and nonlinear ones [45].

2.2. PT symmetry in four-level coherent atomic media

Then, the creation of PT-symmetry was considered in a four-level atomic system by Sheng *et al* as shown in figure 3(a) [46]. In this proposal, a signal field E_s (frequency ω_s, electric-field intensity E_s), a coupling field E_c (ω_c, E_c), and a pump field E_p (ω_p, E_p) excite transitions $|1\rangle\leftrightarrow|3\rangle$, $|2\rangle\leftrightarrow|3\rangle$, $|1\rangle\leftrightarrow|4\rangle$, respectively, which forms an N-type four-level configuration. To achieve the PT-symmetry requirement, two coupled waveguide structures are established under the EIT condition. One of the waveguides provides Raman gain [47] while the other one provides loss/absorption by setting proper parametric conditions for the coupling and pump beams. All the beams propagate along the z direction, as shown in figure 3(b).

The susceptibility of the atomic medium can be obtained through $\chi = \frac{2N\mu_{13}}{\varepsilon_0 E_s}\rho_{31}$, where the density-matrix element ρ_{31} describes the transition property between $|1\rangle\leftrightarrow|3\rangle$ driven by the signal field. The real and imaginary refractive indices for the signal field can be obtained through $n_R \approx \chi'/2$ and $n_I \approx \chi''/2$ respectively. First, the authors realize a standard PT-symmetric potential with a pair of waveguides coupled. They arrange two coupling fields (with an identical Gaussian intensity profile) from two independent laser sources side by side (along the transverse x direction), and the susceptibility experienced by the signal field E_s is modulated as a function of the intensities of the two coupling fields. By choosing different coupling frequency ($\Delta_c = \omega_s - \omega_{32}$) for each
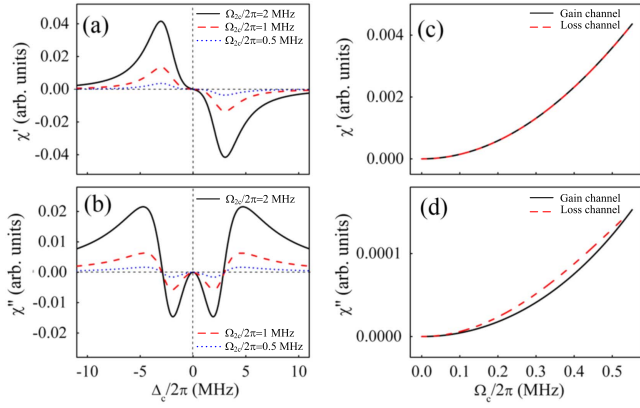
Figure 4. Dependence curves of the real (a) and imaginary (b) parts of the susceptibility χ on the frequency detuning Δ_c at different Rabi frequency Ω_c. The other parameters are taken as $\Delta_s = \Delta_p = 0$, $\Omega_s/2\pi = 0.1$ MHz, $\Omega_p/2\pi = 6$ MHz, $\Gamma_{31}/2\pi = \Gamma_{32}/2\pi = \Gamma_{41}/2\pi = \Gamma_{42}/2\pi = 3$ MHz, $\Gamma_{21} = \Gamma_{43} = 0$. Dependence curves of the real part χ' (c) and imaginary part χ'' (d) on the coupling intensity. The adopted frequency detuning is $\Delta_c/2\pi = -2.939$ MHz (-3.045 MHz) for the gain (loss) waveguides.

Figure 5. Constructed refractive indices as a function of x for cases of (a) below, (b) above the symmetry-breaking threshold, and (c) non-PT-symmetric one. The coupling detunings are $\Delta_c/2\pi = -2.97$ MHz and -3.01 MHz for the respective gain and loss channels in (a); $\Delta_c/2\pi = -2.94$ (gain channel) and -3.04 MHz (loss channel) in (b); and $\Delta_c/2\pi = -2.992$ MHz in (c). Other parameters are the identical as in figure 4 except that the atomic density is set as $\sim 10^{13}$ cm^{-3}. Pictures (d)–(f) and (g)–(i) give the field modes and propagation features of the injected signal beam corresponding to the situations in (a)–(c), respectively.

waveguide, as a consequence, the required gain can be generated inside in one waveguide while loss/absorption in the other one. Based on the two coupled optical waveguides with respective gain and loss, PT-symmetric potentials can be promisingly realized.

To this end, it is very important to identify the dependency of the modulated susceptibility on the frequency detuning of the coupling field on account that the different coupling frequency detunings can lead to different dispersion and gain/loss properties in the two channels. Figures 4(a) and (b) show the evolutions of real and imaginary parts of χ, respectively, by varying the coupling detuning at different coupling intensities. The imaginary component χ'' is approximately 0 (no gain and no absorption) when the coupling detuning is about -2.939 MHz, as shown in figure 4(b), and the absorption (positive susceptibility) and gain (negative susceptibility) can be induced on the left point and right point near this zero location, respectively. Consequently, with the other parameters being the same, the difference between the coupling frequency detuning in the two channels can result in the susceptibilities with different signs for the two coupled waveguides. Also, the dependency of χ on the coupling intensity is shown in figures 4(c) and (d), where the real parts at two selected coupling frequency overlap quite well, while the imaginary parts are not matched perfectly. This implies that one can also construct a perfect PT-symmetry potential by choosing certain Rabi frequency for the coupling fields.

Based on the above analysis, one can achieve the desired spatial modulation on the refractive index. According to the evolution curves in figures 4(c) and (d), one can obtain the corresponding index landscapes as figure 5, in which the real and imaginary parts behave as even and odd functions of the transverse coordinate x. It is worth mentioning that the absolute values of the real and imaginary parts can increase equally with the atomic population, which is set as 10^{12} cm^{-3}
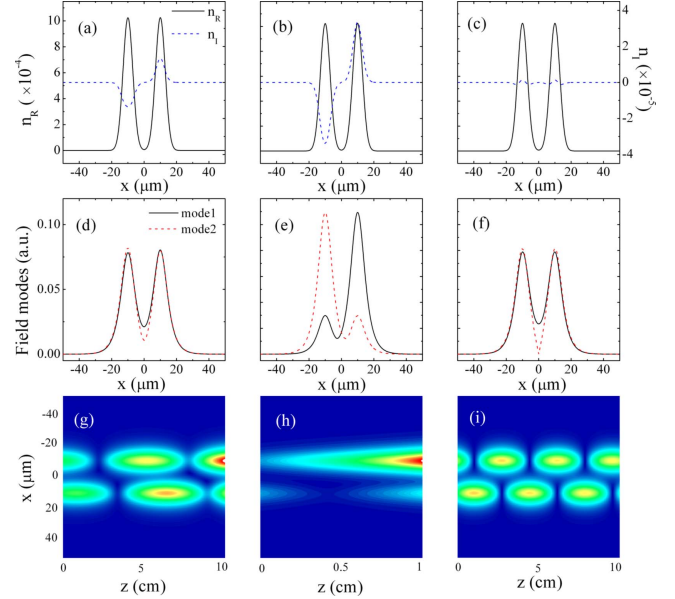
in the current work. To demonstrating the different behaviors for the lights traveling through the waveguide system below and above the PT-symmetric threshold, the ratio n_R/n_I should be effectively controlled [4].

To change the ratio between the real and imaginary indices, the coupling frequency detunings at the two channels are tuned to modify the real and imaginary indices simultaneously as determined by the Kramers–Kronig relations [48]. When detunings Δ_c is set away from $\Delta_c/2\pi = -2.992$ MHz, the system can be operated in the cases of below (figure 5(a)), above (figure 5(b)) threshold and a non-PT-symmetric one (figure 5(c)), corresponding to the ratio of $n_R/n_I = 38$, 15 and 410, respectively.

The corresponding field modes (eigenvectors) in the coupled waveguide system shown in figures 5(a)–(c) are depicted as figures 5(d)–(f), respectively. The modes for the case below threshold (figure 5(a)) should be symmetric and the corresponding eigenvalues should be real. However, due to the imperfect symmetry of the real and imaginary indices of the system, the two modes are slightly asymmetric, as shown in figure 5(d), and the eigenvalues have a tiny imaginary part. Such asymmetric modes are not caused by the PT symmetry breaking. When the PT symmetric condition is broken, i.e., the case above the threshold, as shown in figure 5(b), the modes become severely asymmetric and each mode is confined in its corresponding waveguide, i.e., gain or absorption waveguide, respectively, as shown in figure 5(e). Meanwhile, the eigenvalues become complex and the corresponding imaginary part gives the gain or absorption for
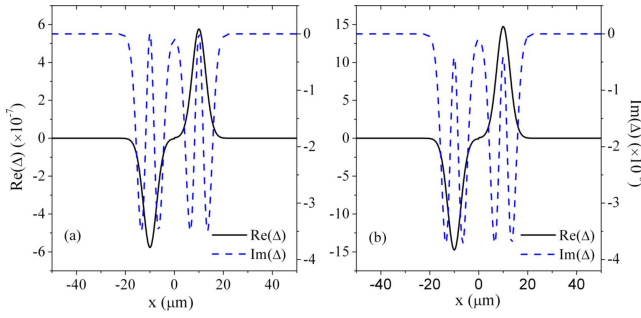
Figure 6. The asymmetric function for the real (solid curves) and imaginary (dashed curves) parts of the refractive index calculated using realistic parameters for (a) below and (b) above threshold cases, as shown in figures 5(a) and (b), respectively.

Figure 7. The distribution of the refractive index for periodic PT-symmetric potential with both the intensity and detuning of the coupling field spatially modified. (a) and (b) are the cases below and above PT symmetric threshold, respectively.

Figure 8. The real (n_R) and imaginary (n_I) parts of the refractive index for PT-symmetric lattice by spatially modulating the coupling- and pump-field intensities.

each mode. For the passive case (figure 5(c)), the modes are perfectly symmetric, as shown in figure 5(f).

The propagation characteristics of the signal beam through the index structures in figures 5(a)–(c) are given as figures 5(g)–(i), respectively. For the case of below threshold, as shown in figure 5(g), the injected beam oscillates periodically between the two coupled waveguides, similarly to the beam dynamics in a passive coupler. By gradually increasing the gain/loss contrast to operate the system above the symmetry breaking threshold, the light dynamics (an exponentially growing mode) is shown as figure 5(h). Finally, figure 5(i) depicts the light dynamics in a pair of coupled passive waveguides (without gain or loss). One can see that the periods of oscillation are different in the PT-symmetric and passive potentials.

To theoretically design an exact PT-symmetric optical potential, perfectly symmetric real index and anti-symmetric imaginary index are required to demonstrate corresponding optical properties. However, in practical experiment, such an ideal PT-symmetry system is not easy to be obtained. Here, we would like to consider how imperfect symmetric and anti-symmetric parts of the index will affect the desired PT-symmetric properties. The deviation from a perfect symmetry/anti-symmetric function is defined as $\Delta(x) = n(x) - n^*(-x)$.

Based on the above analysis, the aim is to make the deviation $\Delta(x)$ be close to 0 by properly choosing parameters. Figure 6 shows the deviation from the symmetric/anti-symmetric functions for the real index and imaginary index shown in figures 5(a) and (b), respectively. From figure 6, one can see that the degrees of deviation for the real and imaginary parts are several percents. Therefore, it should not have significant impact in practical experiments.

Next, additional laser beams are introduced to form a periodical optical potential, as shown in figure 7(a). Here, the case for positive coupling detuning is considered, so that the real part of the refractive index becomes smaller as the coupling intensity increases. The ratio n_R/n_I in figure 7(a) is approximately 6.9, which is below PT-symmetric threshold. In figure 7(a), the coupling detuning is simply moved far away from the zero point, which can unfortunately increase the asymmetry of the real index.
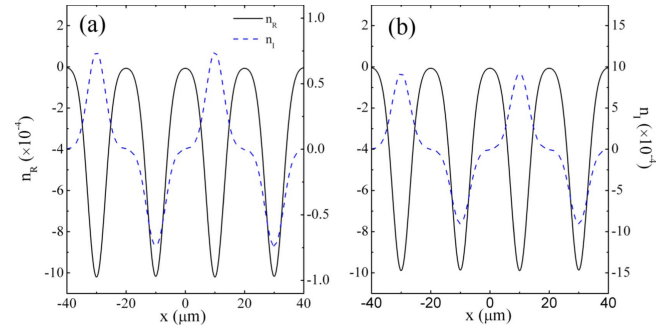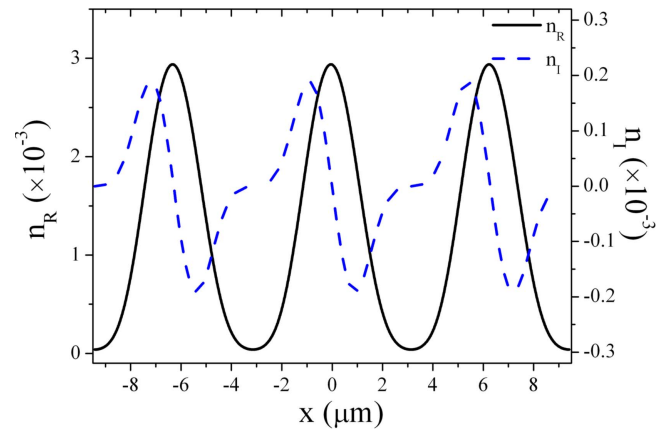
Different pump intensities are adopted in the gain and loss channels to minimize the asymmetry $\Delta(x)$ in the lattice potential. The corresponding parameters for generating the gain (absorption) in figure 7(a) are $\Delta_c/2\pi = 2.882$ (3.102) MHz and $\Omega_p/2\pi = 6$ MHz, while others are the same as that in figure 5. Figure 7(b) shows the case above threshold and the ratio n_R/n_I is about 0.5, which can be manipulated by properly setting different coupling detunings and the pump intensities.

An other way to generate this peoridical PT-symmetric optical potentials is employing contiously-vaying coupling and pump intensities in order to construct the desired real and imaginary parts as shown in figure 8, where each waveguide is filled with half gain and half absorption and the ratio n_R/n_I is about 1.5, which can be modified by the coupling and pump intensities to be below and above the threshold.

In addition, with the intensities of the coupling and pump fields modulated in a two-dimention (2D) manner (along both the x and y directions), one can obtain an extended 2D PT-symmetric lattice potential shown in figure 9 by utilizing of the parametric regimes in figure 8.

In the meanwhile, Wu and his colleagues theoretically constructed the periodic PT symmetry with atomic lattices driven in a four-level cold atomic cloud [36]. The four-level
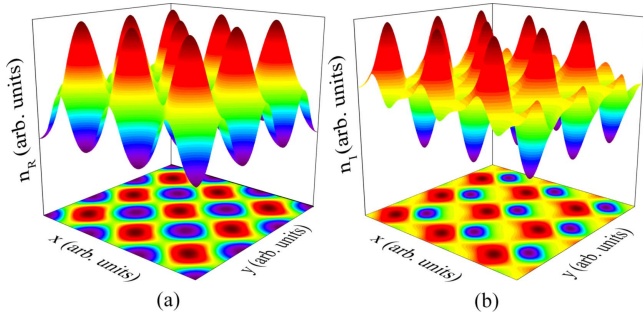
J. Phys. B: At. Mol. Opt. Phys. **51** (2018) 072001

Topical Review

Figure 9. Distribution of the refractive index for a 2D PT-symmetric optical lattice. Reprinted figure with permission from [46], Copyright (2013) by the American Physical Society.
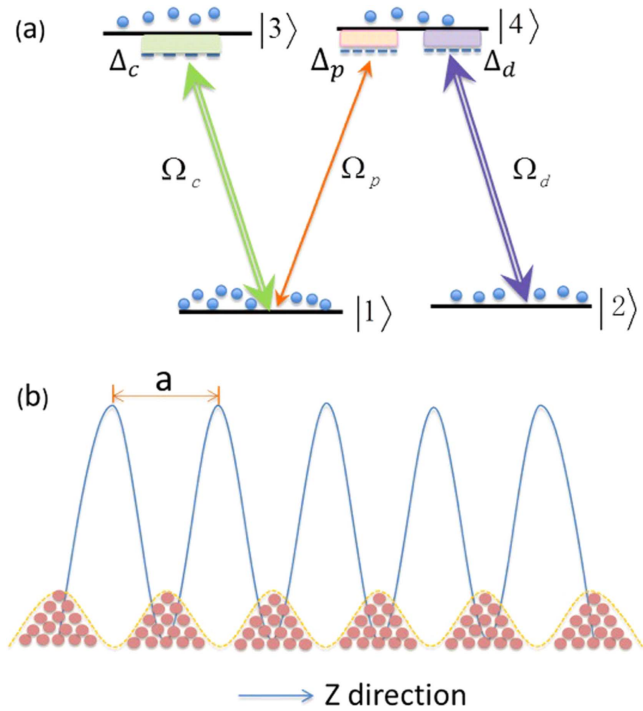

Figure 10. (a) Diagram of a four-level N-type energy-level structure in a cold atomic cloud, which involves a probe field $\boldsymbol{E}_p$ (Rabi frequency Ω_p, electric-field intensity E_p), a strong coupling field $\boldsymbol{E}_c$ (Ω_c, E_c), and a driving field $\boldsymbol{E}_d(\Omega_d, E_d)$. (b) The population of an atomic ensemble is modulated as a periodical distribution by an 1D trapping optical lattice. The atomic population in each trapping channel is assumed to exhibit a Gaussian distribution. Reproduced with permission from [36].
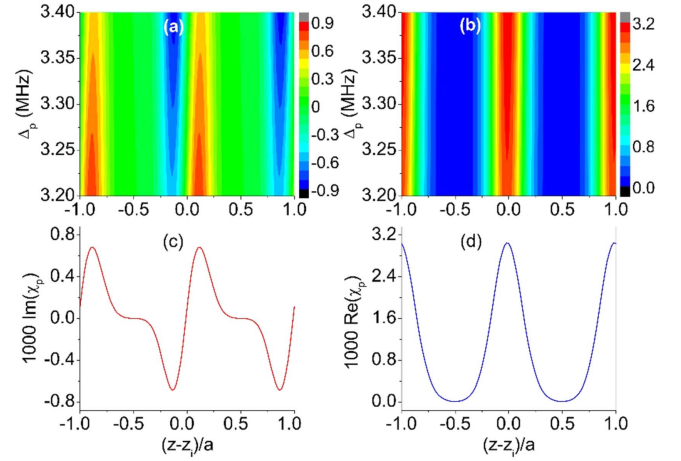

Figure 11. (a) Evolutions of the imaginary and (b) real components of probe susceptibility χ_p versus the position $(z - z_i)/a$ and probe-field detuning Δ_p. (c) Imaginary and (d) real parts of χ_p versus $(z - z_i)/a$ with detuning being $\Delta_p = 3.284$ MHz. The other parameters are $\Omega_{c0} = 3.0$ MHz and $\delta\Omega_c = 0.3$ MHz. Reproduced with permission from [36].

optical lattice for modulating the atomic population. The 2D pictures at the upper two panels in figure 11 clearly show that χ_p'' and χ_p' can be modified in the z direction. One can find that, from the 1D plots at the two lower panels, χ_p'' and χ_p' obey odd and even profiles, respectively, with respected to the lattice (numbered i) center $z = z_i$ when the detuning is set as $\Delta_p = 3.284$ MHz. This directly advocates that the PT-symmetric optical potential is realized in terms of χ_p. The alternation of $\chi_p'' > 0$ in one half period and $\chi_p'' < 0$ in another half period indicate a simultaneously gain and loss. Accordingly, by choosing proper coupling parameters, the induced gain and loss can be balanced for desired PT symmetry.

Based on the above analyzation, the researchers theoretically proposed two different schemes for realizing periodical PT-symmetric optical potential in four-level atomic configurations. These four-level configurations can be potentially applied to construct PT-symmetry potential in experiment by making some modifications according to the practical experimental requirements.

2.3. Anti-PT symmetry with atoms

With the notion of PT symmetry extensively investigated in various optical settings, its counterpart anti-PT symmetry, which obeys $n(x) = -n^*(-x)$, is also demonstrated in optics. Anti-PT symmetry requiring no optical gain can display many fascinating features, such as spontaneous phase transition of the scattering matrix, a flat total transmission band, a continuous lasing spectrum [50] and unidirectional reflectionlessness [33], which may open up new opportunities for manipulating light and form a complementary probe in non-Hermitian optics. Recently, anti-PT symmetry with a pair of coupled components was firstly implemented in a multi-level atomic configuration depending on the multi-parameter tunable property and coherent nature [51]. Considering that controlling the coupling strength between two optical modes in an atomic system is much more difficult than in a solid-state system, Xiao's group

system shown in figure 10 is consisted of two ground states $|1\rangle$ and $|2\rangle$ and two excited states $|3\rangle$ and $|4\rangle$. A probe field $\boldsymbol{E}_p$ couples the transition $|1\rangle \leftrightarrow |4\rangle$, and two strong pump fields $\boldsymbol{E}_c$ and $\boldsymbol{E}_d$ connect $|1\rangle \leftrightarrow |3\rangle$ and $|2\rangle \leftrightarrow |4\rangle$, respectively. Given that the density of cold atoms possesses a Gaussian distribution in each channel of the lattice for trapping the 1D periodical atomic distribution, this PT-symmetric lattice is constructed by modulating intensity or frequency detuning of one driving field in a sinusoidal manner (inducing a spatially periodic Stark shift of $|2\rangle$) [49].

In their work, the authors study the real (χ_p') and imaginary (χ_p'') components of the susceptibility for the probe field (shown in figure 11) in two neighboring channels of the

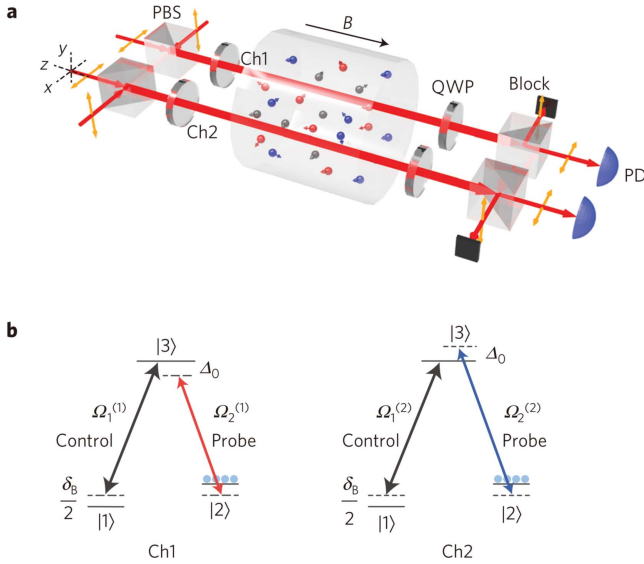J. Phys. B: At. Mol. Opt. Phys. **51** (2018) 072001

Topical Review

Figure 12. (a) Schematic for realizing anti-PT symmetry via rapid atomic-coherence transport in a thermal ^{87}Rb vapor cell. Two spatially separated optical channels (Ch1 and Ch2) each contains collinearly propagating weak probe and strong controlling fields operating under the condition of EIT. The output probe transmission spectra are measured by sweeping a homogeneous magnetic field generated by a solenoid inside a covering layer, which can shield the ambient magnetic field. PD: photodiode detector, PBS: polarization beam splitter, QWP: quarter-wave plate. (b) The three-level Λ-type EIT configurations in two channels. All the probe and controlling fields with orthogonal circular polarizations come from an external cavity diode laser. Reprinted by permission from Macmillan Publishers Ltd: [Nature Physics] [51], Copyright (2016).

uses the thermal motion of warm atoms to construct the coupling between the two optical modes.

The experiment is operated in an ^{87}Rb atomic vapor cell with the temperature set at about 40°C, as shown in figure 12(a). The inner surface of the cell is coated with coherence-preserving paraffin [52], which allows atoms to undergo thousands of wall collisions with little demolition of their internal quantum state. The atomic vapor cell is housed within a four-layer covering shield to screen out the ambient magnetic field. Inside the covering layer, a solenoid is used to generate a uniform magnetic field, which can induce a Zeeman shift δ_B on the two-photon detuning. One laser beam from an external cavity diode laser (ECDL) is spatially split into four beams with half-wave plates and polarization beam splitters. The probe and controlling lights (with orthogonally linear polarizations) are first recombined and converted to circular polarization by quarter-wave plates (QWP), and then directed into two optical channels (named as Ch1 and Ch2) with a distance of 1 cm between them.

The energy-level configuration of Ch1 and Ch2 are shown in figure 12(b), where two right-circularly polarized strong-control fields ($\Omega_1^{(1)}$ and $\Omega_1^{(2)}$) couple the transition $|1\rangle \leftrightarrow |3\rangle$, and two left-circularly polarized weak-probe fields ($\Omega_2^{(1)}$ and $\Omega_2^{(2)}$) connect the transition $|1\rangle \leftrightarrow |3\rangle$. For the steady-state condition, the population mainly locates in level $|2\rangle$. The frequency of the two probe fields are shifted with the same one-photon detuning $|\Delta_0|$ (but with opposite signs) by using

acoustic optical modulators. Here Δ_0 is the frequencies difference between the probe and controlling fields. In each channel, the co-propagating probe and controlling fields establish a Λ-type EIT window and create a ground-state coherence with a long lifetime of $\sim$100 ms. Such an arrangement can effectively couple the two spin waves by the random and irreversible atomic motion, which distributes atomic coherence through the optically thin medium and is the foundation for generating the non-Hermiticity for the effective Hamiltonian.

Theoretically, based on the density-matrix formalism [53] for describing the atom–light interaction, the time-dependent non-Hermitian Hamiltonian H_{eff} is obtained to describe the dynamics of the two collective spin-wave excitations. The resonance condition of the coupled system is met when $\text{Det}[H_{\text{eff}}] = 0$, whose solutions coincide with the two eigenvalues of H, defining the appearance of the two Eigen-EIT supermodes (in terms of δ_B). Here δ_B is a parameter that is swept to extract the eigenvalues of H. Since H satisfies $\hat{P}\hat{T}H = -H$ (i.e., $[H, \hat{P}\hat{T}] = 0$) in contrast to $\hat{P}\hat{T}H = H$ (i.e., $[H, \hat{P}\hat{T}] = 0$) for the conventional PT symmetry, H in the current system is considered as an anti-PT -symmetric Hamiltonian. In addition, this anti-PT-symmetric H leads to a phase transition exhibited on the two Eigen-EIT spectral branches. Specifically, in the symmetry-unbroken regime ($|\Delta_0| < \Gamma_c$), the two Eigen-EIT resonances coincide at the center $\delta_B = 0$, but with different linewidths. The breaking point occurs at $|\Delta_0| = \Gamma_c$, where the two supermodes perfectly overlap. When $|\Delta_0| > \Gamma_c$, the driven system runs under the symmetry-broken regime, and the resonances bifurcate and exhibit level anti-crossing, resembling a passively coupled system.

The spectral profiles of the two eigen-EIT spectra were experimentally obtained by slowly scanning the magnetic field with time and measuring the weak-probe transmission. To experimentally extract the linewidth and line center of the eigen-EIT spectra from the measured beating patterns, one must identify the beating note with the maximal amplitude and choose its peak location as the time reference origin. Starting from this reference point, the remaining discrete time points are then sequentially identified at distances of integral multiples of the beating period. Figures 13(a) and (b) show the observed probe transmission depending on both δ_B (lower x-axis) and time (upper x-axis), and the corresponding beating pattern, to be specific, two sets of representative probe transmission spectra with $\Delta_0 = \mp15$ Hz (figures 13(a1) and (a2)) under the symmetry-unbroken regime and $\Delta_0 = \mp60$ Hz (figures 13(b1) and (b2)) under the symmetry-broken regime. From the beating spectra, one can extract a set of EIT spectra, as denoted by the red/blue dots. The spectra are fitted (red/blue lines) by a weighted sum of the two Eigen-EIT spectra to give the line-width and line center values as predicted.

At the same time, the evolution of the anti-PT supermodes below and above the exceptional point is carefully examined by varying $|\Delta_0|$. The centers and corresponding linewidths of the extract lines are a function of $|2\Delta_0|$, as shown in figure 13. Remarkably, the current system has a
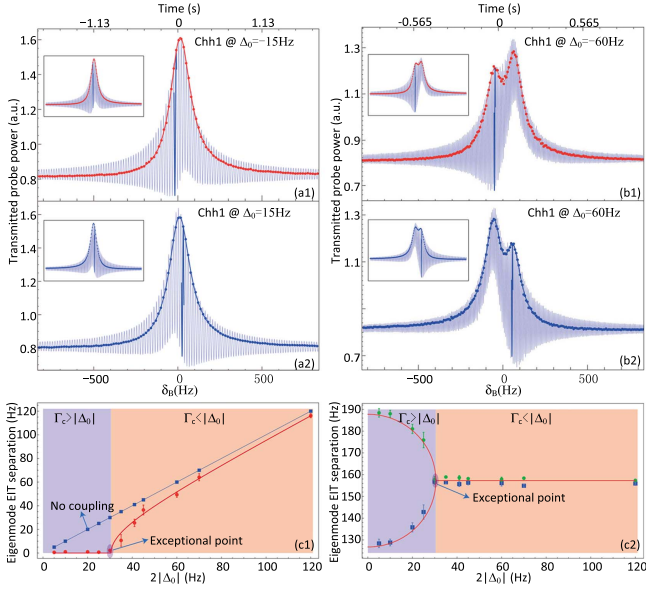
J. Phys. B: At. Mol. Opt. Phys. **51** (2018) 072001

Topical Review

Figure 13. (a1), (a2) Transmission spectra of the probe light from Ch1 and Ch2 (with respective probe detuning ∓15 Hz) in the regime of symmetry-unbroken case, respectively. (b1), (b2) Transmission spectra of the probe light with detuning set as ∓60 Hz in Ch1 and Ch2, respectively, in the regime of symmetry-broken case. The bold, dotted curves in (a1), (a2), (b1), and (b2) are the EIT spectra extracted at time points, and the beating notes marked in dark blue are for the phase reference. The insets are calculated curves from the theory. (c1), (c2) The real part $Re[\omega]$ (c1) and imaginary part $Im[\omega]$ (c2) of the two eigen frequencies of the coupled-EIT supermodes versus the probe detuning $|\Delta_0|$. In (c1), the blue squares represent the EIT peak separation between two uncoupled channels, and the red dots are for the coupled case. In (c2), the green dots and blue squares are the extracted linewidths of the two eigen-EIT modes, respectively. Reprinted by permission from Macmillan Publishers Ltd: [Nature Physics] [51], Copyright (2016).

high resolution of the phase-transition threshold at the Hz level, which may open up new avenues for precisely measuring the optical phase or the magnetic field.

The promising experiment based on a coherently-prepared multi-level atomic configuration offers a versatile environment for investigating the properties of anti-PT symmetry in optical field. The photon-photon interaction can be modified from linear to nonlinear by choosing proper experimental parameters. Moreover, given the tight connection of the current system to magnetometers, slow light and quantum memory [54], new directions may be opened up for precision measurements, quantum optics and quantum information science.

Besides the study on anti-PT symmetry with two coupled components, Wu *et al* theoretically predicted the non-Hermitian degeneracies and unidirectional reflectionlessness in a 1D Bragg grating, where the periodical probe susceptibility χ_p satisfies $\chi_p(-z) = -\chi_p^*(-z)$ with loss and no gain [33, 55]. In this work, cold Rb atoms are captured as a 1D lattice by a periodical dipole traps formed by the counter-propagating red-detuned lasers with the same wavelength of λ_0, as shown in figure 14(a). The periodicity of the trapped atomic lattice can be calculated as $a = 0.5\lambda_0 / \cos\theta_0$, where θ_0 is the angle between laser beams forming the trapping lattice and the z
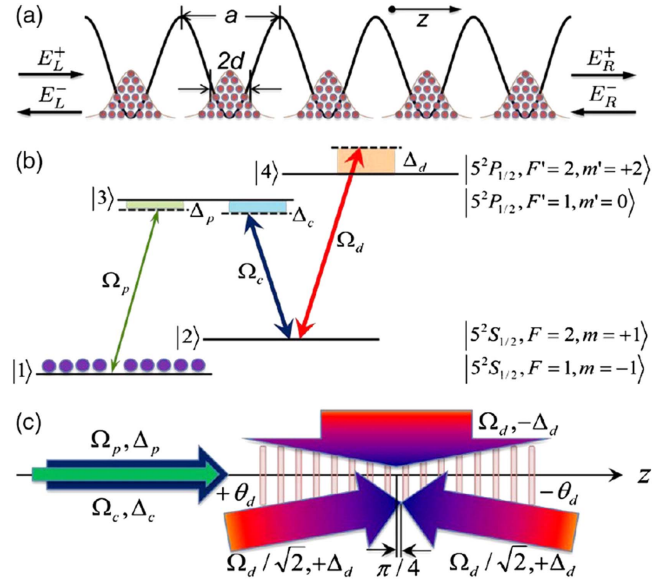

Figure 14. (a) The distribution of a cold ^{87}Rb atomic ensemble is modulated by a 1D periodical lattice and the trapped atoms in each channel possess a Gaussian density distribution (b) energy-level structure of an N-type atomic configuration. (c) Possible geometry for the suggested scheme. Reprinted figure with permission from [33], Copyright (2014) by the American Physical Society.

direction. The atomic population in each channel of the induced lattice has a Gaussian distribution. The atoms are coherently driven to connect an *N*-type configuration shown in figure 14(b) by a weak probe E_p (frequency ω_p, Rabi frequency Ω_p), a coupling field E_c (ω_c, Ω_c) and a strong dressing field E_d (ω_d, Ω_d). The experimental scheme is shown as figure 14(c). The probe (σ^+ polarization) and coupling (σ^- polarization) fields propagate along the same z direction. The dressing field is split into three components, and two of them (both σ^+ polarization) counter-propagate in a very small angular offset $\pm\theta_d$ (with respect to the z direction) to spatially modify the light shift $\delta_{dz}(z)$ corresponding to transition $|2\rangle \leftrightarrow |4\rangle$, while the third component (linearly polarization in the y direction) propagates along the x direction to provide a light shift.

According to the rotating-wave approximations, density matrix element ρ_{31} can be obtained under the approximation of $\rho_{11} \approx 1$. The probe susceptibility $\chi_p(z)$ satisfying $\chi_p(z) = -\chi_p^*(-z)$ can be achieved by spatially arranging the critical parameters of atom–light interacting system [35, 56]. Considering that the atomic density distribution is an even function of the lattice position, one can set the frequency shift δ_{d0} as an odd one by taking the dressing field with three components (with σ^+ polarization). So, the probe susceptibility can be modulated in every channel of the atomic lattices.

The modulated real and imaginary parts of susceptibility χ_{pj} versus the lattice position z and probe frequency detuning are given as figures 15(a) and (b), respectively. The frequency detunings in the current configuration are defined as $\Delta_p = \omega_p - \omega_{31}$, $\Delta_c = \omega_c - \omega_{32}$ and $\Delta_d = \omega_d - \omega_{42}$. And the evolution of χ_{pj} at different Ω_d is calculated in figures 15(c) and (d). As can be seen from figure 15, the refractive index induced in the periodical atomic lattices satisfy the condition
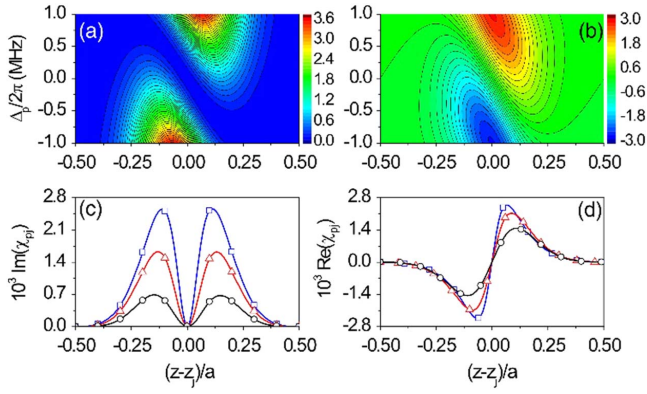
Figure 15. (a), (b) Im(χ_{pj}) and Re(χ_{pj}) depending on the lattice position $(z - z_j)/a$ and probe detuning $\Delta_p/2\pi$. (c), (d) Im(χ_{pj}) and Re(χ_{pj}) versus $(z - z_j)/a$ at $\Delta_p = 0$ with $c/2\pi$ set as 16 MHz (circles), 22 MHz (triangles), 28 MHz (squares). Reprinted figure with permission from [33], Copyright (2014) by the American Physical Society.

of anti-symmetry $\chi_{pj}(+z) = -\chi_{pj}^*(-z)$ when $\Delta_p = 0$. However, the anti-symmetry is gradually moved up with the increasing of $|\Delta_p|$, as seen from figures 15(a) and (b). Based on the non-Hermitian degeneracies, this work also predicts the unidirectional reflectionless propagation of laser. The unidirectional vanishing probe reflectivity can be easily controlled by setting proper dressing-field parameters.

3. Spatially periodic coherent optical effect

Up to now, the experimental observations of (anti-)PT symmetry are mainly completed in a pair of coupled optical configurations such as waveguides and microcavities [57]. Considering that even a single PT unit can possess fantastic optical features, the non-Hermitian optical lattices are extensively studied to show more new behaviors and properties [5, 8, 9, 14–16, 23, 33, 39, 45, 58–66]. The theoretical studies show that a non-Hermitian lattice can lead to novel properties including optical solitons [23, 39], non-Hermitian Bloch oscillations [8, 9], unidirectional invisibility [15], PT-symmetric Talbot effect [63], double refraction, and nonreciprocal characteristics [5], which may provide new thoughts for exploring non-Hermitian synthetic materials. Fortunately, the first experimental study on periodic PT symmetry with gain and loss are achieved based on spatially periodical coherent effect in a multi-level atomic configuration. In the following, we will give a summary to show the recent progresses on periodical optical potential based on atomic coherence.

3.1. Dipole soliton in laser-induced atomic gratings

Firstly, the charged dipole-mode solitons are studied in high-order nonlinear processes generated in coherent multi-level atoms with electromagnetically induced grating (EIG) structures, where the Kerr nonlinearities are dramatically strengthened [67]. The key point for experimentally obtaining such dipole-mode solitons is to induce a high-contrast periodical refractive index inside the atomic medium. As a
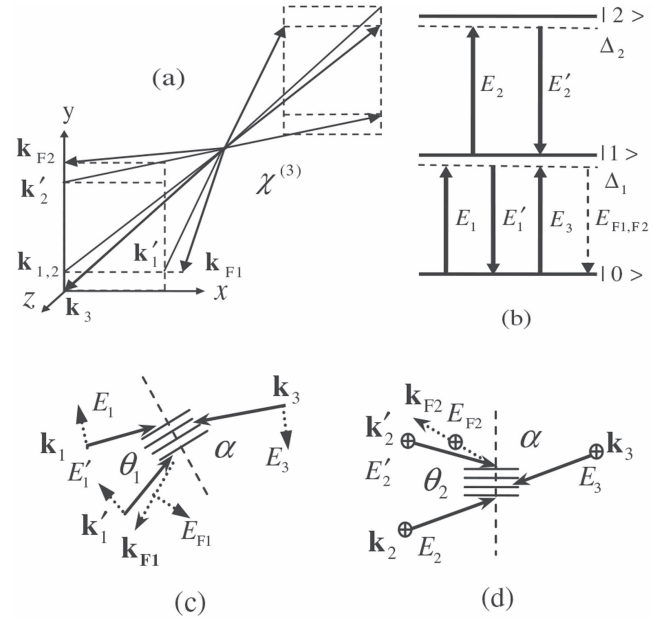

Figure 16. (a) Beam arrangement for the experiment. (b) The energy-level structure for generating FWM E_{F1} and E_{F2}. (c) E_{F1} with TM polarization and (d) E_{F2} with TE polarization are manipulated through the induced EIG1 and EIG2, respectively. Reprinted figure with permission from [67], Copyright (2011) by the American Physical Society.

consequence, two-component dipole-mode solitons are effectively produced in two coexisting four-wave mixing (FWM) processes. Such observed spatial solitons can lead to the wave-guiding effect with the assistance of the non-linearity-induced focusing effect.

In that system, two EIGs are established under the geometrical configuration shown as figure 16(a) and energy-level system as figure 16(b). Two optical fields E_1 and E_1' (frequency ω_1, Rabi frequency Ω_1 and Ω_1', respectively) propagate in the same direction with an angle of $\theta_1 \approx 0.3°$ between them to connect the transition $|0\rangle \leftrightarrow |1\rangle$. A weak probe field E_3 (ω_1, Ω_3) propagates along the opposite direction of E_1. Two additional coupling fields E_2 and E_2' (ω_2, Ω_2 and Ω_2', respectively) link the transition $|1\rangle \leftrightarrow |2\rangle$. As a result, the beams E_1 and E_1' (E_2 and E_2') can induce the grating EIG1 (EIG2), which is schematically given as figure 16(c) (figure 16(d)).

Such periodical refractive index can establish two photonic band gaps (PBGs) [68, 69], which can lead to the prohibition of the probe transmission and therefore, the reflections with high efficiency. Thus, the dipole-like FWM $E_{F1}(E_{F2})$ can be viewed as the diffraction patterns of the incident probe laser E_3 from the horizontally-aligned EIG1 (vertically-aligned EIG2). Furthermore, the generated FWM signals and probe field can form a vector soliton.

Experimentally, the dressing fields (Ω_1', Ω_1 or Ω_1' together with Ω_1) can impose influence on the generated FWM E_{F2} in such cascaded three-level system, and different dressing settings are shown in figure 17(a). The transverse nonlinear phase shift ϕ_2 generated by EIG2 can result in two dipole patterns.

For the points Δ_1 with weak dispersion effect, E_{F2} beam is only modulated linearly. For the points $|\Delta_1| = 16.5$ GHz
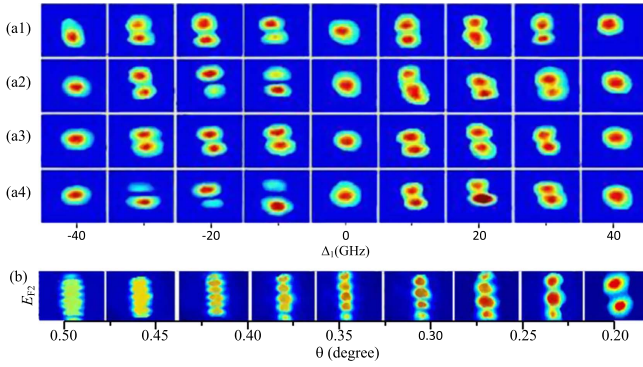
J. Phys. B: At. Mol. Opt. Phys. **51** (2018) 072001

Topical Review

Figure 17. (a1)−(a4) Images of dipole-soliton E_{F2} at different Δ_1 in the cascaded three-level system with $\Omega_2' = \Omega_2 = 20$ GHz, $\Omega_1' = 55$ GHz and $\Omega_1 = 45$ GHz (a1), $\Omega_1' = 55$ GHz and $\Omega_1 = 0$ (a2), $\Omega_1' = 0$ and $\Omega_1 = 45$ GHz (a3), and $\Omega_1' = 0$ and $\Omega_1 = 0$ (a4). (b) Bragg reflections of E_{F2} beam at different θ_2. The parameters are $\Delta_1 = -15$ GHz, $\Delta_2 = -4.5$ GHz, $\Omega_1' = \Omega_1 = \Omega2' = \Omega_2 = 20$ GHz, and $\Omega_3 = 0.5$ GHz. Reprinted figure with permission from [67], Copyright (2011) by the American Physical Society.

(where exists the maximum $|n_2|$), the balanced interplay between the diffraction and the cross-Kerr nonlinearity results in the vertically-oriented dipole soliton [67]. In the range from $\Delta_1 = -30$ GHz to $\Delta_1 = -10$ GHz, where appears the self-focusing effect, the energy in the two elements of the E_{F2} dipole mode is effectively exchanged. For the points at resonance or large frequency detuning, the E_{F2} soliton evolves into an common one without node. Under the situation of enhanced FWM due to dressing, the coexisted Ω_1' and Ω_1 can exert a greater effect on E_{F2} than the single (with only Ω_1' or Ω_1 on) and no dressing (with both Ω_1' and Ω_1 off) cases. Further, with the angle θ_2 between the beams E_2 and E_2' decreasing, as shown in figure 17(b), the diffracted fringes decrease from eight (at $\theta_2 = 0.5°$) to two (at $\theta_2 = 0.2°$), since the spatial periodicity of EIG2 increases with the decreasing θ_2. This work experimentally generates the spatial diffraction pattern based on high-order nonlinearity and opens the way for spatially modulating the propagation of lights in atomic settings and potentially studying the periodic non-Hermitian potential in nonlinear optics.

3.2. Discrete diffraction patterns in an optically-induced lattice

With dipole-mode solitons investigated in dressed nonlinear processes, the discrete diffraction based on EIT technique (linear response) is also experimentally demonstrated, which provides an effective solution to generate a waveguide array. The experimental setup is shown in figure 18(a). A probe field ($\lambda_p = 780$ nm, ω_p, Rabi frequency Ω_p) and a pair of coupling fields ($\lambda_c = 776$ nm, ω_c, Ω_c) connect a three-level ^{87}Rb atomic system as shown in figure 18(b), which consists of $5S_{1/2}(|1\rangle)$, $5P_{3/2}(|2\rangle)$ and $5D_{5/2}(|3\rangle)$. A pair of elliptical-shaped coupling beams from a Ti: Sapphire ring laser co-propagate with a small angle of $2\theta \approx 0.4°$ and drive the transition $|2\rangle \leftrightarrow |3\rangle$. As a result, a standing wave associated with the PBG is established along the transverse x direction. The periodicity of the standing-wave field is calculated as $d = \lambda/(2\sin\theta) \approx 112$ μm. The Gaussian probe laser counter-propagating with the two coupling lasers can cover the optical
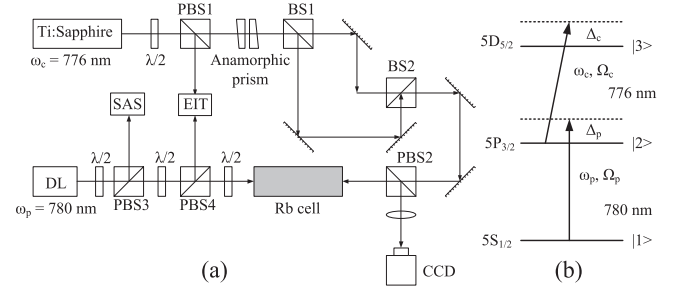

Figure 18. (a) Experimental setup for generating discrete diffraction in an atomic vapor cell. PBS: polarization beam splitter; BS: beam splitter; DL: external cavity diode laser; SAS: saturation absorption spectroscopy; EIT: the setup for monitoring the two-photon EIT window; $\lambda/2$: half-wave plate; CCD: charge coupled device camera. (b) The relevant three-level rubidium atomic system. Reproduced with permission from [70].
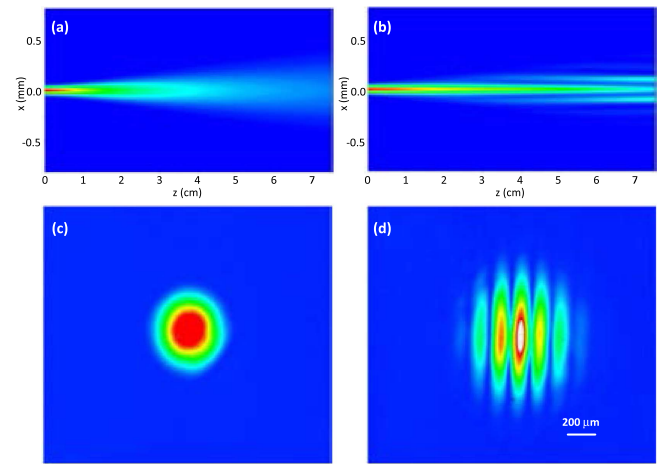

Figure 19. (a) Theoretically standard diffraction of a Gaussian beam without the coupling lattice. (b) Evolved discrete diffraction of a Gaussian light through an optical lattice by theoretical simulations. (c) Experimentally output Gaussian probe beam without the coupling optical lattice. (d) Observed output image when the probe field propagates through the cell with the coupling lattice turned on. Reproduced with permission from [70].

lattice (induced by the standing-wave coupling field) inside the medium. The probe field propagating through the lattice is imaged onto a charge coupled device (CCD) camera.

By employing the beam propagation method [5], the diffractions of a week Gaussian probe laser passing through the medium without and with an optical lattice are theoretically given as figures 19(a) and (b), respectively. Obviously, in the presence of the standing-wave coupling field (optical lattice), the incident probe laser can be discretized.

The experimentally observed output images of the probe field are displayed in figures 19(c) and (d) with the optically-induced lattice turned on and off, respectively. As shown in figure 19(c), the output probe field remains a Gaussian profile, which agrees well with the theoretical picture in figure 19(a) with only normal diffraction. With the standing-wave field on, as shown in figure 19(d), the output of the probe beam appears as stripe patterns due to the discrete diffraction. The adjacent bright channels in figure 19(d) have the same space
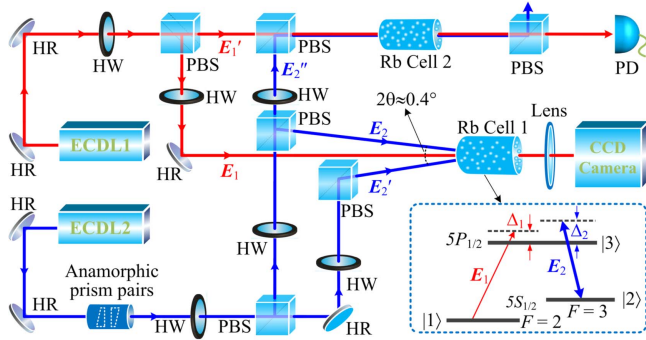
J. Phys. B: At. Mol. Opt. Phys. **51** (2018) 072001

Topical Review

Figure 20. Experimental setup and the relevant three-level Λ-type atomic system (in the dashed box). An imaging lens is applied to observing the probe beam via a CCD camera with. Beams E_1' and E_2'' are injected into the auxiliary cell2 to generate an EIT window in the frequency domain to calibrate the frequencies of the lasers. ECDL: external cavity diode laser, HW: half-wave plate, HR: high-reflectivity mirror, PBS: polarization beam splitter, PD: photodiode detector. Reprinted figure with permission from [71], Copyright (2018) by the American Physical Society.

Figure 21. (a) The diffracted probe images at various z distances. (b) Dependence of the Talbot length on the angle θ. The squares represent the experimentally measured Talbot length while the solid curve represents the theoretical ones. Reprinted figure with permission from [71], Copyright (2018) by the American Physical Society.

Figure 22. Observed fractional Talbot effect (double periodicity) at $z = 8$ mm ($\approx Z_T/2$) and $z = 22$ mm ($\approx 3Z_T/2$). The experimentally observed integer Talbot length is $Z_T \approx 15$ mm. Reprinted figure with permission from [71], Copyright (2018) by the American Physical Society.

as that in the induced lattice. Such experimental results provide a solid foundation in studying PT-symmetric lattice in atomic medium and the travel of light through optical lattices.

3.3. Electromagnetically induced Talbot effect

Inspired by the scheme for generating diffraction patterns with the assistance of an optically-induced lattice [70], the electromagnetically induced Talbot effect (EITE) [71, 72] has been experimentally demonstrated in a three-level atomic system. This provides the possibility to realize PT-symmetric Talbot effect [63] by adding an additional pump field to construct the PT-symmetry potential [73].

The experimental setup for EITE and corresponding energy-level structure are shown in figure 20. The probe field E_1 (wavelength $\lambda_1 = 794.97$ nm, frequency ω_1, horizontal polarization, and Rabi frequency Ω_1) from a single-mode tunable ECDL1 co-propagates with two coupling beams to drive a Λ-type ^{85}Rb atomic configuration (see figure 20(a)). The three-level structure consists of two hyperfine ground states, i.e. $5S_{1/2}$ $F = 2$ (state $|1\rangle$) and $F = 3$ (state $|2\rangle$), and one excited state $5P_{1/2}$ (state $|3\rangle$). Two elliptically shaped coupling beams, E_2 and E_2' ($\lambda_2 = 794.97$ nm, ω_2, vertical polarization, and Ω_2 and Ω_2', respectively) from ECDL2 with the same angle of $\theta = 0.2°$ regarding the z axis intersect at the center of the cell, and induce an optical lattice (with a periodicity of $d = \lambda_2/2\sin\theta \approx 114$ μm) along the transverse x.

By carefully choosing the experimental parameters for the probe and coupling fields, the diffraction pattern of the probe beam from the induced EIG [74] can be clearly observed at the output plane of the cell. The diffraction pattern is monitored by a CCD camera equipped with an imaging lens, which is similar to the setup used in section 3.2. In addition, by coupling two beams E_1' and E_2'' into a second auxiliary cell2 to establish a same Λ-type EIT spectrum for reference, one can calibrate the frequencies of the fields E_1 and E_2 [41].

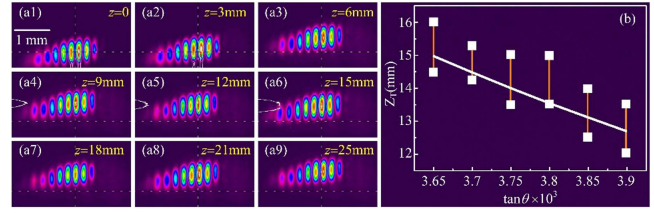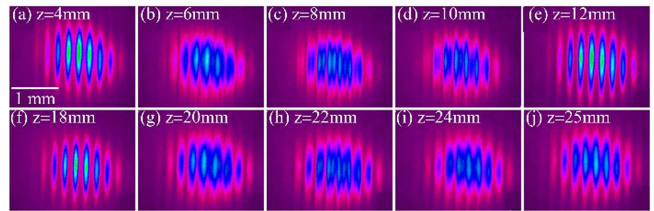The propagation characteristic feature of the EIG-diffracted probe field out of the cell is obtained by the CCD

camera equipped with an imaging lens. By moving the lens (placed on a precision translation stage) together with the CCD camera (fixed on another translation stage) to maintain the distance between them (along the z direction) to be twice the lens's focal length, one can obtain the imaging results at different observing planes with high accuracy. The observed images at different distances along the z direction are shown in figures 21(a1)–(a9). The experimental results show that the diffracted image shifts by a half period (compared to that at $z = 0$) when the observation plane is set to be $z \approx 15$ mm, which is close to the theoretically predicted Talbot length of $Z_T = 16.3$ mm [72]. Additionally, figure 21(b) shows the experimentally measured dependence of the Talbot length on angle 2θ, which determines the periodicity of the coupling standing wave as well as the optical lattice. For a given angle 2θ, two measured values exist (maximum and minimum values), showing a range in which the recurrence effect seems to be optimal. The experimental observations match well with the theoretical solid curve, which advocates that the periodicity of the lattice indeed determines the Talbot length.

Figure 22 demonstrated the observed fractional Talbot effect. The periodicity of the discretized probe beam at $z = Z_T/2$ and $z = 3Z_T/2$ is doubled while the intensity is dramatically weakened. The period-doubled images occur at nearly $z = 8$ mm ($\approx Z_T/2$) and $z = 22$ mm ($\approx 3Z_T/2$), which coincide with the theoretical calculation.

Although this EITE is implemented in an atomic vapor cell, this effect will work effectively in cold atoms, considering that EIG has already been experimentally demonstrated in cold sodium atoms under EIT conditions [75]. When extended to cold atomic samples, the angle 2θ can be increased to reduce the EIG period d since the Doppler effect

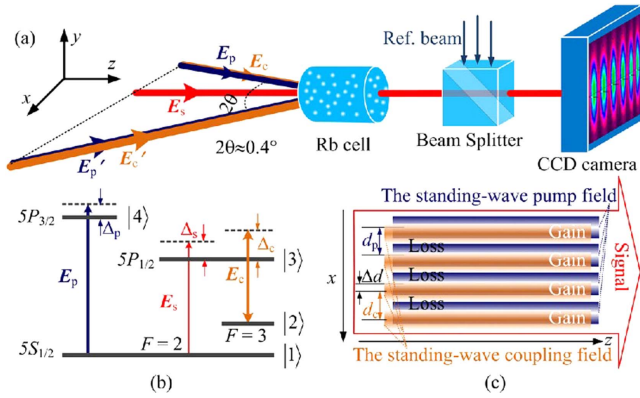J. Phys. B: At. Mol. Opt. Phys. **51** (2018) 072001

Topical Review

Figure 23. (a) Experimental setup. The output gain and loss and the relative phase difference are detected by a CCD camera. Two pump lasers E_p' and E_p come from the same external cavity diode laser (ECDL), while the two coupling beams E_c' and E_c from another ECDL. The reference beam from the same ECDL as E_s is introduced by a 50/50 beam splitter. (b) The energy-level structure driven in ^{85}Rb atomic vapor. (c) The spatial beam geometry of the three fields inside the medium. x and z represent the transverse and longitudinal directions of light propagation, respectively. With the distance Δ_d between the two lattices optimized, we can observe the gain and loss alternately along the x direction for the signal beam. Reprinted figure with permission from [73], Copyright (2016) by the American Physical Society.

can be negligible. Therefore, this well established system is an ideal platform to investigate interesting nonlinear/quantum beam dynamics predicted in artificial periodic optical systems beyond the EITE due to its controllable linear absorption/dispersion and nonlinear properties.

4. PT symmetry in a reconfigurable gain–loss optical array

The recently proposed notion of periodical non-Hermitian potential in optics has spawned intriguing prospects. The known experimental work on a periodic PT-symmetric optical potential is finished in an lossy optical waveguide array formed in the solid-state environment, which involves loss and no-loss channels only, i.e. without gain [61]. Namely, PT symmetry has not yet been observed in a spatially extended periodic gain–loss optical lattice, as discussed in [76]. Such observation is delayed due to various limitations of solid-state structures including the restrictions in generating gain in certain materials and the connection between the real and imaginary indices as imposed by Kramers–Kronig relations [48]. Recently, the PT symmetry in gain–loss modulated optical lattice has been achieved in a four-level atomic configuration [73].

The experiment setup and corresponding four-level N-type atomic configuration are shown in figures 23(a) and (b), respectively. The signal field E_s and the standing-wave coupling and pump fields, i.e. two intersecting strong coupling lasers E_c and E_c' and two intersecting strong pump lasers E_P and $E_{P'}$, propagate in the same z direction to drive the N-type four-level configuration in a ^{85}Rb atomic
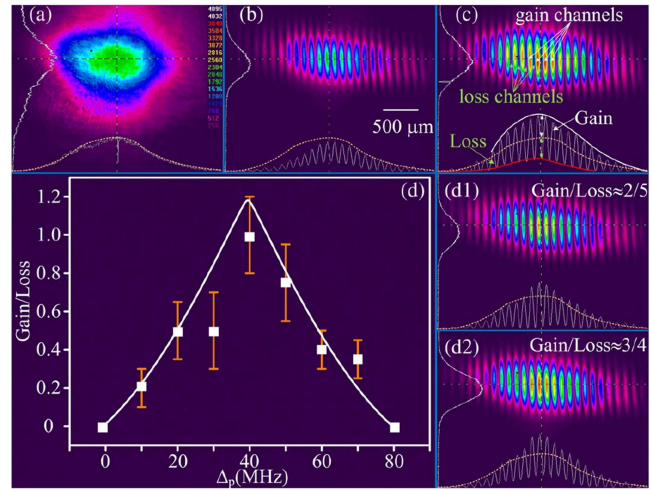

Figure 24. The measured periodical gain and loss regions on the probe-field image (a) The Gaussian image and intensity profile of the signal field E_s without absorption or gain. (b) Beam E_s after passing through the coupling lattice with the pump field turned off. (c) Generated simultaneous gain and loss profiles when the signal beam propagates through the coupling and pump lattices. (d) Evolution of the gain and loss profiles by discretely changing the pump detuning Δ_p. The squares representing the experimental observations can match well with the theoretical solid curve. The measured gain and loss profiles at $\Delta_p = 30$ MHz (d1) and 10 MHz (d2). Reprinted figure with permission from [73], Copyright (2016) by the American Physical Society.

ensemble, which is the same as energy level used in the theoretical proposal in [46]. By carefully setting the experimental conditions, the essential active Raman gain for realizing exact PT-symmetric optical potential can be effectively generated on the weak field E_s [32, 47]. In experiment, two elliptical-Gaussian coupling beams (shaped by an anamorphic prism pair) E_c and E_c' from the same ECDL (of wavelength $\lambda_c = 794.97$ nm) are injected into the cell in the same manner as the EITE experiment to construct an optical lattice. The space between two neighboring bright fringes of coupling lattices is $d_c = \lambda_c/2\sin\theta \approx 114\,\mu$m. Similarly, two pump beams E_p and E_p' ($\lambda_p = 780.24$ nm), partially overlapped with E_c and E_c', respectively, are incident into the medium to induce a pump-field optical lattice. The 7 cm long vapor cell is wrapped with μ-metal sheets to shield the magnetic field. The signal beam E_s ($\lambda_s = 794.97$ nm) with a Gaussian intensity profile passes through the two partially overlapped optically-induced lattices (with an adjustable spatial-shift distance Δd between them), as shown in figure 23(c).

By spatially modulating the intensity of the coupling field, the real (dispersion) and imaginary parts of the refractive index for the signal field are spatially modulated as a function of the transverse coordinate x under the EIT scheme in the Λ-type subsystem $|1\rangle \rightarrow |3\rangle \rightarrow |2\rangle$ [70]. Next, the imaginary part can alternately appear either above (absorption/loss) or below (gain) zero along x with the intensity-modulated pump field turned on. With the Gaussian signal beam shown in figure 24(a) traveling through the coupling lattice, one can obtain obvious discrete diffraction patterns that depict the spatial modification on the refractive index experienced
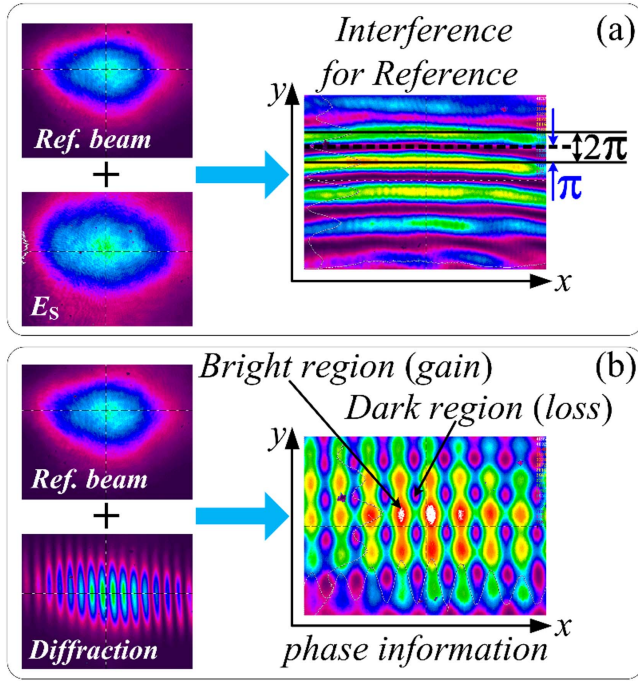
Figure 25. (a) The interference pattern of $\boldsymbol{E}_s$ and the reference beam (injected along the y direction). They are from the same ECDL. The phase difference between the two solid lines is 2π. The phase difference between the black dotted line (located at the middle point between the two solid lines) and one of the two solid lines is π. (b) The interference pattern between the intensity-modulated $\boldsymbol{E}_S$ field (after diffraction) and the reference beam, so that the square lattice is formed. Reprinted figure with permission from [73], Copyright (2016) by the American Physical Society.

Figure 26. (a) Experimental evolutions of the phase difference ν at different γ_G/γ_L. (b) Theoretically calculated ν in a PT-symmetric lattice with ten waveguides coupled. The propagation distance is set as $z = 10$. Reprinted figure with permission from [73], Copyright (2016) by the American Physical Society.

by the signal field in the EIT-medium. Such stripe patterns can be observed when the frequency detuning is within a window of 50 MHz around the two-photon resonance, i.e. $\Delta_s - \Delta_c = 0$ [70, 71]. Figure 24(b) shows the diffraction pattern, which is obtained by carefully adjusting d_c at $\Delta_s - \Delta_c = 10$ MHz and $\Delta_s = -100$ MHz.

In principle, the EIT modulated signal field $\boldsymbol{E}_s$ can be amplified with the presence of pump field. Consequently, the pump-field lattice can introduce alternative gain and loss (with a high and controllable contrast) on the output signal beam with different coupling- and pumping-field intensities arranged, which can be achieved by carefully modifying the space Δd between the two partially overlapped lattices (see figure 23(c)). As one can see in figure 24(c), two neighboring channels on the spatially extended periodic probe beam appear gain and loss. The dotted curve in figure 24 represents the original intensity of the incident signal beam before entering the medium. The gain/loss ratio between two adjacent channels in figure 24(c) is approximately 1, i.e. a case with equalized gain and loss, which is necessary for constructing an exact PT symmetry in coupled waveguide systems [5]. Figure 24(d) depicts the dependence of the gain/loss ratio on the pump detuning Δ_p. The theoretical prediction (solid curve) based on numerical calculation agrees well with the experimental observations (squares). Figures 24(d1) and (d2) show the generated gain and loss profiles with the detuning tuned to $\Delta_p = 30$ MHz and 10 MHz, respectively.
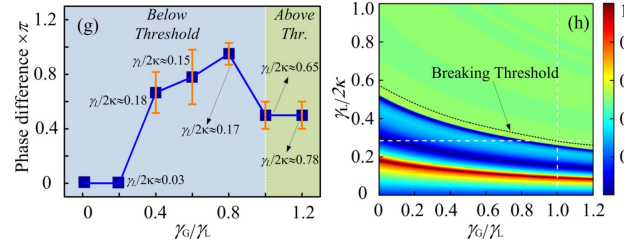
The manifestation of the constructed PT-symmetric system below or above the symmetry-breaking threshold can be to look at the relative phase difference ν between two adjacent gain and loss channels, which represents the internal phase difference of the eigenvectors [13] and can reflect the attributes of the system. Figure 25 shows the measurement of the explicit phase difference generated in two adjacent channels with respective gain and loss. The phase difference between two maximums of the adjacent interference fringes is 2π, i.e. the distance of the double-sided arrow between the two solid lines, as shown in figure 25(a). The distance mentioned here is along the y direction. The space (marked by a pair of one-way arrows) between one of the two solid lines and the dotted line represents a phase difference of π. With the gain and loss array generated, the reference interference can modulate the well arranged gain and loss regions as a net-like lattice composed of 'bright' and 'dark' squares (corresponding to gain and loss channels, respectively), which can be easily understood through the schematic diagram shown in figure 25(b). The mentioned relative phase difference (proportionally to the relative distance along the y direction) depends on the gain/loss ratio.

Figure 26(a) exhibits the experimentally measured phase difference at various gain/loss ratios. The case with no phase difference, i.e. $\nu = 0$, is detected with the gain being zero. When the gain is introduced, the phase difference ν ($\nu \neq 0$) is observed as the ratio γ_G/γ_L increases from 0.4 to 0.8, which remains below the phase transition point. For the situation above the breaking threshold, as one can see in figure 26(a), the measured ν stays unchanged as γ_G/γ_L continuously increases from 1 to 1.2. The dependence between the observed ν and ratio γ_G/γ_L can be reasonably understood by the theoretical pictures as shown in figure 26(b), which demonstrates that term $\gamma_L/2\kappa$ can effectively affect the phase difference for a given γ_G/γ_L. Considering that the coupling coefficient κ between two selected waveguides is directly determined by n_R, term $\gamma_L/2\kappa$ indicates the evolution of n_I/n_R, which can mathematically determine the transition point of the non-Hermitian optical system [46].

According to the experimental conditions for a certain gain/loss ratio in figure 26(a), one can calculate the value of $\gamma_L/2\kappa$, which determines the state (below or above the threshold) of the gain- and loss-modulated array obeying PT symmetry by solving the coupling equations [73]. In

principle, even if the gain/loss ratio is not perfectly balanced in a coupled-waveguide lattice system, i.e., $\gamma_G/\gamma_L \neq 1$, the characteristic eigenvalue pattern is simply shift regarding the zero line for a balanced case [77, 78]. Consequently, such a quasi-PT-symmetric system with an unbalanced gain and loss can also demonstrate the dynamical behaviors of its exact PT-symmetry counterparts.

This work, for the first time, experimentally demonstrated a spatially extended PT-symmetric optical lattice with controllable gain/loss ratio in a coherently-prepared atomic ensemble. The PT-symmetry required refractive index modulation and the anti-symmetric gain/loss profiles are realized by employing the EIT and active Raman gain in the four-level N-type atomic configuration. Due to the large available parametric space, the refractive index and gain/loss profiles modulated by the two sets of optical lattices can be easily tuned/controlled and reconfigured in real time. The currently established variable optical waveguide array with alternate gain/loss channels would be very hard to realize in solid-state systems. Consequently, such a constructed PT-symmetric optical lattice can provide a promising platform to investigate diverse effects involving non-Hermitian Hamiltonians, including periodical anti-PT-symmetric potential and non-Hermitian-modulated Talbot effect [63], and PT-symmetric photonic Floquet topological insulators.

5. Summary

Non-Hermitian optics has attracted the attention of researchers from various fields since the exploitation of the mathematical isomorphism existing between the quantum Schrödinger and the paraxial wave equations. The unique propagating features of light in non-Hermitian optical settings have undoubtedly inspired extensive theoretical and experimental studies. After a decade of efforts, the principles of optical systems for demonstrating non-Hermitian Hamiltonian are fairly well understood. Particularly, the extension of the related phenomenon to atomic field, considering the reconfigurability in real time and tunability with a large set of parameters, provides a new platform to study non-Hermitian Hamiltonians under different parametric regimes, which not only enriches the perspectives in theory but also paves the routes for a variety of potential applications. The light-induced atomic coherence can result in easily controllable absorption, dispersion, Raman gain, and nonlinearity, which can be applied to experimentally construct real-time tunable coupled waveguides and realize the interplays between non-Hermitian optical potential and Kerr nonlinearity. Actually, a lot of fascinating non-Hermitian optical properties [38–40] have been theoretically proposed with coupled waveguides and nonlinearity involved. From this point of view, we will not be surprised that new observations on non-Hermitian optical phenomenon will continue to appear in coherently-prepared atomic media.

ORCID iDs

Zhaoyang Zhang ⓘ https://orcid.org/0000-0001-9207-0927
Yanpeng Zhang ⓘ https://orcid.org/0000-0002-0954-7681

References

[1] Bender C M and Boettcher S 1998 Real spectra in non-Hermitian Hamiltonians having PT symmetry *Phys. Rev. Lett.* **80** 5243–6

[2] Lévai G and Znojil M 2000 Systematic search for PT-symmetric potentials with real energy spectra *J. Phys. Math. Gen.* **33** 7165–80

[3] Bender C M 2007 Making sense of non-Hermitian Hamiltonians *Rep. Prog. Phys.* **70** 947–1018

[4] El-Ganainy R, Makris K G, Christodoulides D N and Musslimani Z H 2007 Theory of coupled optical PT-symmetric structures *Opt. Lett.* **32** 2632–4

[5] Makris K G, El-Ganainy R, Christodoulides D N and Musslimani Z H 2008 Beam dynamics in PT symmetric optical lattices *Phys. Rev. Lett.* **100** 103904

[6] Klaiman S, Guenther U and Moiseyev N 2008 Visualization of branch points in PT-symmetric waveguides *Phys. Rev. Lett.* **101** 080402

[7] Guo A, Salamo G J, Duchesne D, Morandotti R, Volatierravat M, Aimez V, Siviloglou G A and Christodoulides D N 2009 Observation of PT-symmetry breaking in complex optical potentials *Phys. Rev. Lett.* **103** 093902

[8] Longhi S 2009 Bloch oscillations in complex crystals with PT symmetry *Phys. Rev. Lett.* **103** 123601

[9] Wimmer M, Miri M A, Christodoulides D and Peschel U 2015 Observation of Bloch oscillations in complex PT-symmetric photonic lattices *Sci. Rep.* **5** 17760

[10] Fleury R, Sounas D and Alu A 2015 An invisible acoustic sensor based on parity-time symmetry *Nat. Commun.* **6** 5905

[11] Szameit A, Rechtsman M C, Bahat-Treidel O and Segev M 2011 PT-symmetry in honeycomb photonic lattices *Phys. Rev. A* **84** 021806

[12] Fleury R, Sounas D L and Alu A 2014 Negative refraction and planar focusing based on parity-time symmetric metasurfaces *Phys. Rev. Lett.* **113** 023903

[13] Rüter C E, Makris K G, El-Ganainy R, Christodoulides D N, Segev M and Kip D 2010 Observation of parity-time symmetry in optics *Nat. Phys.* **6** 192–5

[14] Regensburger A, Bersch C, Miri M-A, Onishchukov G, Christodoulides D N and Peschel U 2012 Parity-time synthetic photonic lattices *Nature* **488** 167–71

[15] Lin Z, Ramezani H, Eichelkraut T, Kottos T, Cao H and Christodoulides D N 2011 Unidirectional invisibility induced by PT-symmetric periodic structures *Phys. Rev. Lett.* **106** 213901

[16] Yin X and Zhang X 2013 Unidirectional light propagation at exceptional points *Nat. Mater.* **12** 175–7

[17] Feng L, Xu Y L, Fegadolli W S, Lu M H, Oliveira J E, Almeida V R, Chen Y F and Scherer A 2013 Experimental demonstration of a unidirectional reflectionless parity-time metamaterial at optical frequencies *Nat. Mater.* **12** 108–13

[18] Sanchez-Soto L L and Monzon J J 2014 Invisibility and PT symmetry: a simple geometrical viewpoint *Symmetry* **6** 396–408

[19] Peng B, Ozdemir S K, Lei F, Monifi F, Gianfreda M, Long G L, Fan S, Nori F, Bender C M and Yang L 2014 Nonreciprocal light transmission in parity-time-symmetric whispering-gallery microcavities *Nat. Phys.* **10** 394–8

[20] Chang L, Jiang X, Hua S, Yang C, Wen J, Jiang L, Li G, Wang G and Xiao M 2014 Parity-time symmetry and variable optical isolation in active-passive-coupled microresonators *Nat. Photon.* **8** 524–9

[21] Chong Y D, Ge L, Cao H and Stone A D 2010 Coherent perfect absorbers: time-reversed lasers *Phys. Rev. Lett.* **105** 053901

[22] Longhi S and Feng L 2014 PT-symmetric microring laser-absorber *Opt. Lett.* **39** 5026–9

[23] Wimmer M, Regensburger A, Miri M A, Bersch C, Christodoulides D N and Peschel U 2015 Observation of optical solitons in PT-symmetric lattices *Nat. Commun.* **6** 7782

[24] Liang G Q and Chong Y D 2013 Optical resonator analog of a two-dimensional topological insulator *Phys. Rev. Lett.* **110** 203904

[25] Zhen B, Hsu C W, Igarashi Y, Lu L, Kaminer I, Pick A, Chua S-L, Joannopoulos J D and Soljacic M 2015 Spawning rings of exceptional points out of Dirac cones *Nature* **525** 354–8

[26] Zhang Y, Zhong H, Belic M R, Zhu Y, Zhong W, Zhang Y, Christodoulides D N and Xiao M 2016 PT symmetry in a fractional Schrodinger equation *Laser Photonics Rev.* **10** 526–31

[27] Li J, Yu R, Ding C and Wu Y 2016 PT-symmetry-induced evolution of sharp asymmetric line shapes and high-sensitivity refractive index sensors in a three-cavity array *Phys. Rev.* A **93** 023814

[28] Teimourpour M H, Khajavikhan M, Christodoulides D N and El-Ganainy R 2017 Robustness and mode selectivity in parity-time (PT) symmetric lasers *Sci. Rep.* **7** 10756

[29] Teimourpour M H, Ge L, Christodoulides D N and El-Ganainy R 2016 Non-Hermitian engineering of single mode two dimensional laser arrays *Sci. Rep.* **6** 33253

[30] Jahromi A K, Hassan A U, Christodoulides D N and Abouraddy A F 2017 Statistical parity-time-symmetric lasing in an optical fibre network *Nat. Commun.* **8** 1359

[31] Scully M O 1991 Enhancement of the index of refraction via quantum coherence *Phys. Rev. Lett.* **67** 1855–8

[32] Pei L *et al* 2013 Resonant stimulated Raman gain and loss spectroscopy in Rb atomic vapor *Phys. Rev.* A **87** 063822

[33] Wu J H, Artoni M and La Rocca G C 2014 Non-Hermitian degeneracies and unidirectional reflectionless atomic lattices *Phys. Rev. Lett.* **113** 123004

[34] Hang C, Huang G and Konotop V V 2013 PT symmetry with a system of three-level atoms *Phys. Rev. Lett.* **110** 083604

[35] Li H, Dou J and Huang G 2013 PT symmetry via electromagnetically induced transparency *Opt. Express* **21** 32053–62

[36] Wang X and Wu J H 2016 Optical PT-symmetry and PT-antisymmetry in coherently driven atomic lattices *Opt. Express* **24** 4289–98

[37] Chao Hang D A Z, Guoxiang H and Vladimir V K 2016 PT-symmetric waveguides with tunable parameters *IEEE J. Sel. Top. Quantum Electron.* **22** 4402710

[38] Hang C, Zezyulin D A, Konotop V V and Huang G 2013 Tunable nonlinear parity-time-symmetric defect modes with an atomic cell *Opt. Lett.* **38** 4033–6

[39] Abdullaev F K, Kartashov Y V, Konotop V V and Zezyulin D A 2011 Solitons in PT-symmetric nonlinear lattices *Phys. Rev.* A **83** 041805

[40] Ramezani H, Kottos T, El-Ganainy R and Christodoulides D N 2010 Unidirectional nonlinear PT-symmetric optical structures *Phys. Rev.* A **82** 043803

[41] Gea-Banacloche J, Li Y, Jin S and Xiao M 1995 Electromagnetically induced transparency in ladder-type inhomogeneously broadened media: theory and experiment *Phys. Rev.* A **51** 576–84

[42] Sheng J, Yang X, Wu H and Xiao M 2011 Modified self-Kerr-nonlinearity in a four-level N-type atomic system *Phys. Rev.* A **84** 053820

[43] O'Brien C, Anisimov P M, Rostovtsev Y and Kocharovskaya O 2011 Coherent control of refractive index in far-detuned Lambda systems *Phys. Rev.* A **84** 063835

[44] Zezyulin D A, Kartashov Y V and Konotop V V 2011 Stability of solitons in PT-symmetric nonlinear potentials *Europhys. Lett.* **96** 64003

[45] He Y, Zhu X, Mihalache D, Liu J and Chen Z 2012 Lattice solitons in PT-symmetric mixed linear-nonlinear optical lattices *Phys. Rev.* A **85** 013831

[46] Sheng J, Miri M-A, Christodoulides D N and Xiao M 2013 PT-symmetric optical potentials in a coherent atomic medium *Phys. Rev.* A **88** 041803

[47] Kang H, Wen L and Zhu Y 2003 Normal or anomalous dispersion and gain in a resonant coherent medium *Phys. Rev.* A **68** 063806

[48] Horsley S A R, Artoni M and La Rocca G C 2015 Spatial Kramers–Kronig relations and the reflection of waves *Nat. Photon.* **9** 436–9

[49] Turduev M, Botey M, Giden I, Herrero R, Kurt H, Ozbay E and Staliunas K 2015 Two-dimensional complex parity-time-symmetric photonic structures *Phys. Rev.* A **91** 023825

[50] Li G and Türeci H E 2013 Antisymmetric PT-photonic structures with balanced positive- and negative-index materials *Phys. Rev.* A **88** 053810

[51] Peng P, Cao W, Shen C, Qu W, Wen J, Jiang L and Xiao Y 2016 Anti-parity-time symmetry with flying atoms *Nat. Phys.* **12** 1139–45

[52] Robinson H G, Ensberg E S and Dehmelt H G 1958 Preservation of spin state in free atom-inert surface collisions *Bull. Am. Phys. Soc.* **3** 9

[53] Scully M O and Zubairy M S 1997 *Quantum Optics* (Cambridge: Cambridge University Press)

[54] Novikova I, Walsworth R L and Xiao Y 2012 Electromagnetically induced transparency-based slow and stored light in warm atoms *Laser Photonics Rev.* **6** 333–53

[55] Wu J H, Artoni M and La Rocca G C 2015 Parity-time-antisymmetric atomic lattices without gain *Phys. Rev.* A **91** 033811

[56] Horsley S A R, Wu J H, Artoni M and La Rocca G C 2013 Optical nonreciprocity of cold atom Bragg mirrors in motion *Phys. Rev. Lett.* **110** 223602

[57] Christodoulides D N and Miri M A 2014 PT symmetry in optics and photonics *Proc. SPIE* **9162** 91621P

[58] Makris K G, EI-Ganainy R, Christodoulides D N and Musslimani Z H 2010 PT-symmetric optical lattices *Phys. Rev.* A **81** 063807

[59] Dmitriev S V, Sukhorukov A A and Kivshar Y S 2010 Binary parity-time-symmetric nonlinear lattices with balanced gain and loss *Opt. Lett.* **35** 2976–8

[60] Musslimani Z H, Makris K G, EI-Ganainy R and Christodoulides D N 2008 Optical solitons in PT periodic potentials *Phys. Rev. Lett.* **100** 030402

J. Phys. B: At. Mol. Opt. Phys. 51 (2018) 072001

Topical Review

[61] Eichelkraut T, Heilmann R, Weimann S, Stuetzer S, Dreisow F, Christodoulides D N, Nolte S and Szameit A 2013 Mobility transition from ballistic to diffusive transport in non-Hermitian lattices *Nat. Commun.* **4** 2533

[62] Miri M-A, Regensburger A, Peschel U and Christodoulides D N 2012 Optical mesh lattices with PT symmetry *Phys. Rev.* A **86** 023807

[63] Ramezani H, Christodoulides D N, Kovanis V, Vitebskiy I and Kottos T 2012 PT-symmetric talbot effects *Phys. Rev. Lett.* **109** 033902

[64] Bendix O, Fleischmann R, Kottos T and Shapiro B 2009 Exponentially fragile PT symmetry in lattices with localized eigenmodes *Phys. Rev. Lett.* **103** 030402

[65] Regensburger A, Miri M A, Bersch C, Näger J, Onishchukov G, Christodoulides D N and Peschel U 2013 Observation of defect states in PT-symmetric optical lattices *Phys. Rev. Lett.* **110** 223902

[66] Zheng M C, Christodoulides D N, Fleischmann R and Kottos T 2010 PT optical lattices and universality in beam dynamics *Phys. Rev.* A **82** 010103

[67] Zhang Y, Wang Z, Nie Z, Li C, Chen H, Lu K and Xiao M 2011 Four-wave mixing dipole soliton in laser-induced atomic gratings *Phys. Rev. Lett.* **106** 093904

[68] André A and Lukin M D 2002 Manipulating light pulses via dynamically controlled photonic band gap *Phys. Rev. Lett.* **89** 143602

[69] He Q-Y, Xue Y, Artoni M, La Rocca G C, Xu J-H and Gao J-Y 2006 Coherently induced stop-bands in resonantly absorbing and inhomogeneously broadened doped crystals *Phys. Rev.* B **73** 195124

[70] Sheng J, Wang J, Miri M A, Christodoulides D N and Xiao M 2015 Observation of discrete diffraction patterns in an optically induced lattice *Opt. Express* **23** 19777–82

[71] Zhang Z, Liu X, Zhang D, Sheng J, Zhang Y, Zhang Y and Xiao M 2018 Observation of electromagnetically induced Talbot effect in an atomic system *Phys. Rev.* A **97** 013603

[72] Wen J, Du S, Chen H and Xiao M 2011 Electromagnetically induced Talbot effect *Appl. Phys. Lett.* **98** 081108

[73] Zhang Z, Zhang Y, Sheng J, Yang L, Miri M A, Christodoulides D N, He B, Zhang Y and Xiao M 2016 Observation of parity-time symmetry in optically induced atomic lattices *Phys. Rev. Lett.* **117** 123601

[74] Ling H Y, Li Y Q and Xiao M 1998 Electromagnetically induced grating: homogeneously broadened medium *Phys. Rev.* A **57** 1338–44

[75] Mitsunaga M and Imoto N 1999 Observation of an electromagnetically induced grating in cold sodium atoms *Phys. Rev.* A **59** 4773–6

[76] Razzari L and Morandotti R 2012 Optics: gain and loss mixed in the same cauldron *Nature* **488** 163–4

[77] Ornigotti M and Szameit A 2014 Quasi PT-symmetry in passive photonic lattices *J. Opt.* **16** 065501

[78] Lupu A, Benisty H and Degiron A 2013 Switching using PT symmetry in plasmonic systems: positive role of the losses *Opt. Express* **21** 21651–68